

## Self-sculpting of a dissolvable body due to gravitational convection

Megan S. Davies Wykes,<sup>\*</sup> Jinzi Mac Huang, George A. Hajjar, and Leif Ristroph  
*Applied Mathematics Laboratory, Courant Institute of Mathematical Sciences, New York University,  
New York, New York 10012, USA*



(Received 27 September 2017; published 26 April 2018; corrected 7 June 2018)

Natural sculpting processes such as erosion or dissolution often yield universal shapes that bear no imprint or memory of the initial conditions. Here we conduct laboratory experiments aimed at assessing the shape dynamics and role of memory for the simple case of a dissolvable boundary immersed in a fluid. Though no external flow is imposed, dissolution and consequent density differences lead to gravitational convective flows that in turn strongly affect local dissolving rates and shape changes, and we identify two distinct behaviors. A flat boundary dissolving from its lower surface tends to retain its overall shape (an example of near perfect memory) while bearing small-scale pits that reflect complex near-body flows. A boundary dissolving from its upper surface tends to erase its initial shape and form an upward spike structure that sharpens indefinitely. We propose an explanation for these different outcomes based on observations of the coupled shape dynamics, concentration fields, and flows.

DOI: [10.1103/PhysRevFluids.3.043801](https://doi.org/10.1103/PhysRevFluids.3.043801)

### I. INTRODUCTION

The interaction of flowing fluids with shapable solid boundaries determines geological forms across a vast range of scales, from the growth of stalactites [1] to the branching and meandering of rivers [2]. The field of geomorphology seeks to understand the changing face of the Earth and other planetary surfaces, and many of the relevant processes involve the coevolution of flows and boundaries. For example, karst topography occurs when water dissolves limestone, a process that can result in sinkholes and extensive cave systems [3]. Other natural sculptures include streamlined yardangs [4], mushroom-shaped hoodoos [5], and crescentlike dunes [6], and the driving processes may include ablation [7,8], corrosion [9], melting [10–12], erosion [13,14], and dissolution [15–18]. Typically the dynamics involve a complex shape-flow coupling, with the flow influencing the evolution of the solid boundary, which in turn affects the flow field.

The shape of a surface can also provide clues to past conditions, as in inferring the presence of flowing water on Mars due to erosion channels [19] and river islands [20]. Such inferences depend on the nature of the shape evolution process and especially the role played by initial conditions. When the morphology evolves from, but maintains some remnant of, a known initial state, then observations of the present state can aid in geological dating. In weathering erosion, for example, sharp edges tend to be smoothed over time, and jaggedness or roughness can thus indicate relative age of river rocks [21]. On a larger scale, the slopes of eroding terrains generally proceed from steep to gentle over time [22]. Often the initial state does not strongly influence the outcome of a geomorphological process, leading to a universal final form that is insensitive to details of the history. The stereotyped shapes of icicles and stalactites [1,23] or river networks and drainage basins [24] are examples across scales.

---

<sup>\*</sup>Present address: Department of Applied Mathematics and Theoretical Physics, Center for Mathematical Sciences, University of Cambridge, Cambridge CB3 0WA, United Kingdom; [megan.davieswykes@cantab.net](mailto:megan.davieswykes@cantab.net)

While these universal forms are largely independent of initial conditions, they are nonetheless useful in making historical inferences, as illustrated by the example of fluvial morphologies on Mars.

It remains unclear what exactly determines the dependence on initial conditions and for flow-driven processes how shape-flow coupling affects this dependence. Here we show that within the simple problem of dissolution of a solid within a fluid, one observes extreme forms of how the evolution of shape depends on the initial geometry. In particular, we consider dissolvable objects and boundaries formed from hard candy and immersed in what is initially quiescent water. Dissolution leads to density differences, which in turn drive gravitational convective flows that strongly feed back on the dissolution rate and thus the shape dynamics. While removed from any particular geological scenario, these laboratory experiments provide a clean and controlled setting to better understand the effect of dissolution dynamics on shape. In a similar approach, we have recently shown that both erodible and dissolvable bodies in an imposed flow converge to distinct universal shapes regardless of initial form [13,14,25]. For the self-sculpting problem considered here in which no external flow is imposed, we observe two different dependences on initial conditions, with one case involving a complete erasing or loss of memory of the starting shape and the other its near perfect retention.

It has long been known that flows tend to enhance dissolution rates, as is familiar from the everyday example of stirring sugar into coffee or tea. Increasing flow speed tends to decrease the thickness of concentration boundary layers near a dissolvable surface, which increases the flux of material [26]. These theoretical ideas can be incorporated into models that predict dissolution rate, which can be tested experimentally in simplified settings, for example, the sedimentation of spherical salt crystals [18]. In more complex situations, flow-driven dissolution can induce pattern formation, such as the scallops formed on a surface adjacent to a turbulent flow [27] and the fractal-like channels carved within a dissolvable porous medium [17]. Recent work from our group considered the simple case of an object dissolving in a unidirectional flow, showing that the forward face of an object is first sculpted into a round shape which is thereafter maintained during self-similar shrinking [25]. Different starting shapes eventually tend toward the same final shape, an example in which the memory of initial conditions is lost.

Even in the absence of an imposed current, near-body flows can develop near a dissolvable boundary due to buoyancy differences in the fluid. Solutal convection occurs quite generically since fluid with higher concentration of solute is typically of different density from that of the far-field fluid. Previous research into this problem has focused on the underside of a horizontal surface that dissolves, in which the arrangement of dense solution above the less-dense fluid is gravitationally unstable [28]. This results in buoyancy driven flows that cause roughening of the dissolving surface [29,30], and a theory based on turbulent boundary layers was shown to account for the length scale of the surface patterning [31]. Recent research has also suggested that the upper surface of an upright dissolvable body tends towards a paraboloid [32], and a phenomenological model describes the reduction of its radius with time but does not account for the overall shape.

Analogous to dissolution are problems involving the melting of an object due to contact with a fluid, in which case the evolution of the solid boundary is controlled by the transfer of heat rather than solute [33]. Although the heat transfer problem for a boundary of fixed shape is well studied (e.g., [34]), less is known about the coupled shape-flow case. For example, a theoretical model for the initial melt rate on the top surface of a vertical ice cylinder compares favorably with experimental observations [12], but the model assumptions break down once the shape changes significantly. The melting of ice spheres in forced and mixed convection has also been studied experimentally [11], along with ice spheres melting under free convection [35]. A wall of ice melting in a salt stratification results in a series of intrusions of melt water moving outward into the ambient and the surface develops a pattern of ridges and troughs [36].

Building on these previous studies, here we experimentally examine the shape dynamics of a dissolving body in the presence of the self-generated flows caused by buoyancy differences. In Sec. II we describe the basic observations and highlight the marked differences in boundaries that dissolve from below (i.e., the lower surface of a body) versus from above (the upper surface). In

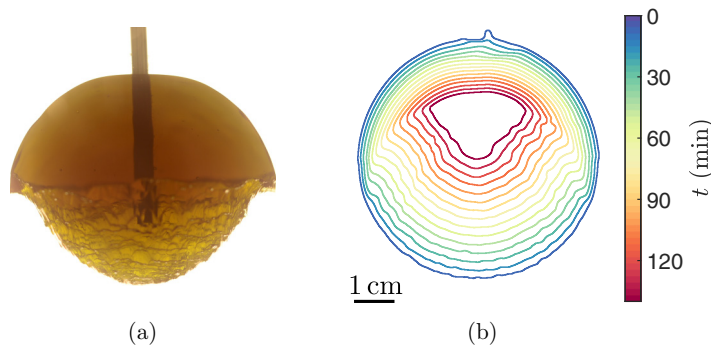


FIG. 1. Shape evolution of a dissolving body. (a) Side-view photograph of candy body (initially a sphere) after dissolution in water for 70 min. (b) Measured profile shape displayed every 10 min. The upper surface remains smooth while the undersurface becomes pitted and dissolves several times faster.

Sec. III we delve more into the behavior of the former, showing that boundaries dissolving from below can retain their initial form, an example of near perfect memory. In Sec. IV we describe the contrasting case of surfaces dissolving from above, where we observe an erasing of the initial shape and tendency toward an ever-sharpening geometry. In Sec. V we use observations and inferences of the shape dynamics, concentration profiles, and flow fields to propose some ideas towards explaining the stark difference in these two cases.

## II. PHENOMENOLOGY: DISSOLUTION OF A SPHERICAL BODY

We begin with experiments that examine the dissolution of what is initially a sphere immersed within a quiescent fluid. The sphere is formed of amorphous solidified sugar [37] (known in the USA as hard candy and in the UK as boiled sweets), made by heating a 8:3:2 mixture by volume of sucrose, light corn syrup, and water to  $150^\circ\text{C}$  and then casting into a mold [25]. Blue or red ink is added to the mixture for visualization purposes and a sphere of initial diameter 6 cm is immersed within water in a  $28 \times 28 \times 28 \text{ cm}^3$  clear tank. The solidified sugar has a measured density of  $1.43 \text{ g/cm}^3$ , which is greater than the density of water  $1.00 \text{ g/cm}^3$ .

As the body dissolves and shrinks, it also changes shape, and a partially dissolved body is shown in Fig. 1(a). There is a clear difference between the upper half, which has remained rounded and smooth, and the lower half, which has become rough and pitted during dissolution. To examine in detail the evolution of shape, photographs are taken at intervals of 20 s using a Nikon D610 digital camera and the scene is lit from behind using a light-emitting diode light pad (Parblo A4S). A time-lapse movie is included in the Supplemental Material as video S1 [38]. The shape of the body over time is shown in Fig. 1(b), where it can be seen from the separation of successive boundaries that the lower half dissolves at a faster rate than the upper half. The upper and lower halves are separated by a cliff or ledge that is seen to form early in the experiment and persist thereafter. The nonuniform shape suggests that fundamentally different dynamics govern these two different regions.

To gain insight into the concentration and flow fields, we perform shadowgraph imaging using a digital projector as a broad and nearly collimated light source behind the dissolving object. The light passes through the tank and casts an image on a translucent screen. In this method, variations in light intensity reflect the dependence of refractive index on dissolved sugar concentration [39]. Time-lapsed photographs of the cast images for  $t = 0, 30, 60, 90,$  and  $120$  min are shown in Fig. 2. Fine-scale intensity variations beneath the body indicate a turbulent jet that descends due to the high concentration of dissolved sugars and thus higher density of this fluid. The dark horizontal line that forms in the fluid near the midheight of the body corresponds to a sharp change in refractive index. This indicates an abrupt change in sugar concentration and corresponds to a density stratification in the fluid, with higher-density fluid sitting below lower-density fluid. As shown in video S2

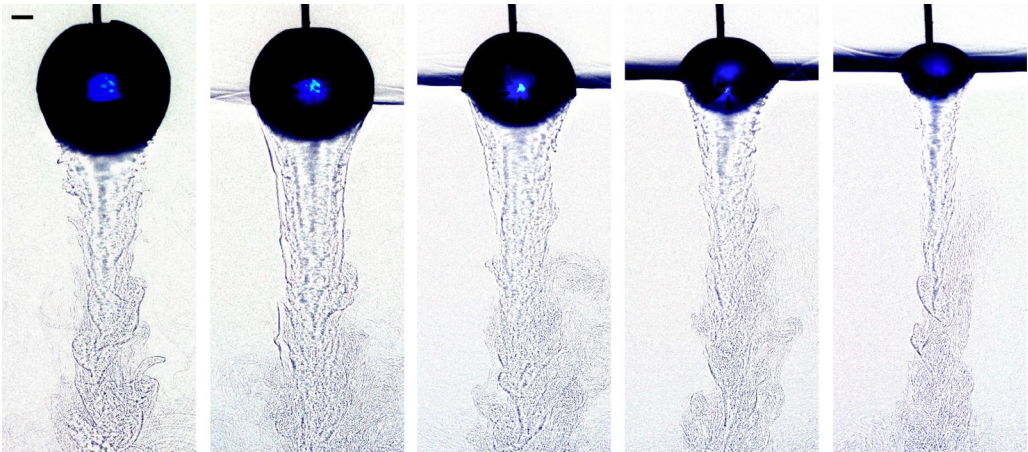


FIG. 2. Shadowgraph images of a dissolution within water at  $t = 0, 30, 60, 90,$  and  $120$  min. The intensity variations beneath the body correspond to a turbulent descending jet of solute-laden fluid. The dark horizontal stripe near the midheight of the body corresponds to the interface of a sharp density stratification. The scale bar is 1 cm.

in [38], this stratification forms over the first 30 min of an experiment as dense sugary fluid that has descended in the jet collects at the bottom of the tank. An interface begins to form at the bottom and rises upward until it nears the midheight of the body, where it remains thereafter.

The height of the stratification corresponds closely to the location of the cliff or ledge on the body, and one might conclude that the formation of the cliff is related to this stratification. To investigate this, we conduct a control experiment in a tank whose far larger volume does not allow for the formation of a sharp stratification. Experiments examining the evolution of the shape are again lit from behind and photographs are taken at intervals of 20 s. In Figs. 3(a) and 3(b) we compare images from the earlier experiments in a smaller tank of volume  $180 \text{ cm}^3$  (top row) and those from the larger tank of volume  $150 \times 10^3 \text{ cm}^3$  (bottom row). Despite the different conditions, the bodies dissolve at the same overall rate and have similar features, including the cliff or ledge. In fact, the only perceptible difference in the two experiments is a slight distortion that appears at the midheight

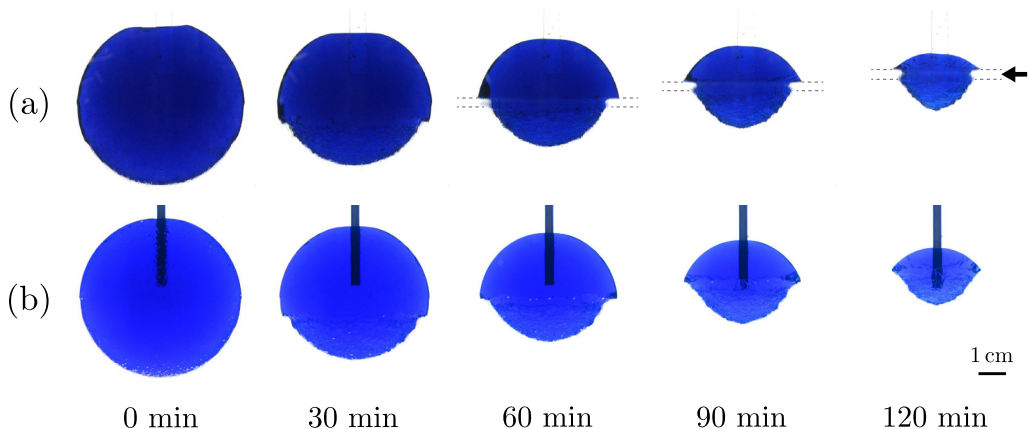


FIG. 3. Tank size has little effect on shape dynamics. Images of dissolving body for (a) tank volume  $180 \text{ cm}^3$  and (b) tank volume  $150 \times 10^3 \text{ cm}^3$ . The stratification interface formed in the smaller tank of (a) causes an optical distortion (dashed lines and arrow) and in reality the bodies are not noticeably different.

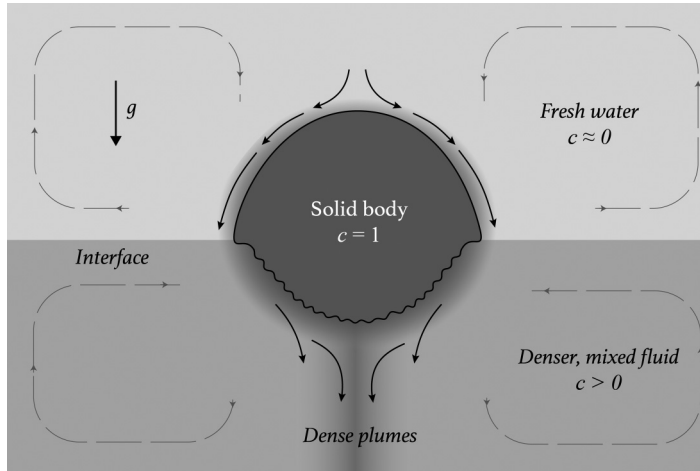


FIG. 4. Interpretation of the buoyancy-driven flow around a dissolving body. Dense solute-laden fluid descends as an attached boundary-layer flow on the upper surface and a highly separated flow over the lower surface. Accumulation of dense mixed fluid in the lower portion yields a sharp stratification. The downward flows induced near the body are matched by broader, slower return flows.

of the body in images at later times for the smaller tank experiments [Fig. 3(a)]. This distortion is an optical artifact due to the sharp interface, causing an apparent concavity in the contour of the body, as indicated by dashed lines and an arrow in Fig. 3(a). That this feature is an imaging artifact is confirmed by inspection of the body upon removal from the tank.

These experiments show that the shape dynamics are not significantly affected by the finite tank size and the consequent change in solute concentration of the far-field fluid during an experiment. A simple calculation suggests that the background concentration is exceedingly small even for the smaller tank. If the entire body were to dissolve into the bottom half of the tank, the concentration would only be 1%.

The shadowgraph visualization studies suggest an interpretation of the flow and concentration fields around the body, as shown in Fig. 4. On the upper side of the body, a thin concentration boundary layer forms as solute diffuses outward from the surface. Due to the higher density of the solute-laden fluid relative to the ambient, a buoyancy-driven flow develops. The flow descends along the upper surface and draws in fresh or low-concentration fluid from above. As it flows from the top of the body to the cliff, the boundary layer is expected to remain attached to the surface, since the arrangement of denser fluid below less-dense fresh fluid is gravitationally stable. Just past the cliff on the underside of the body, this arrangement is reversed, with the dense boundary-layer fluid above the less-dense ambient fluid. The concentration boundary layer is now expected to be gravitationally unstable and here the flow separates off the surface and descends. The entire lower surface is characterized by this arrangement and is thus subject to the Rayleigh-Taylor instability. Fine-scale plumes of dense fluid separate from the surface and combine to form a turbulent jet that rapidly descends to the bottom of the tank. The jet also serves to mix the fluid in the lower portion of the tank and this dense mixture collects to form the stratification and interface. The interface rises within the tank until it reaches the stable-to-unstable transition region, which is the highest point at which solute enters the bulk via boundary-layer shedding. In both the upper and lower layers, volume conservation implies that downward convective flows are matched by broader, slower return flows.

These experiments show a marked difference in the near-body flows and associated shape evolution for a surface dissolving from below (i.e., the lower surface of a body) versus from above (the upper surface). We next consider a series of experiments aimed at better understanding each of these cases separately and with particular focus on the role played by the initial geometry.

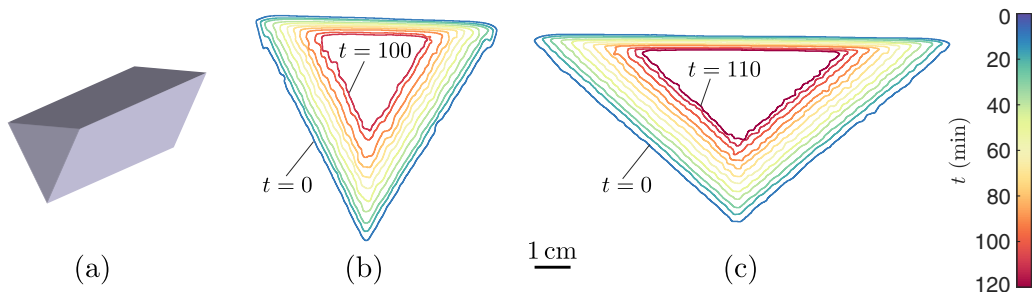


FIG. 5. Shape preservation of dissolving wedges. (a) Sketch of initial configuration: cross-sectional shape evolution at 10-min intervals for bodies with initial base angle (b)  $\theta_0 = 60^\circ$  and (c)  $\theta_0 = 100^\circ$ .

### III. DISSOLUTION FROM BELOW: SHAPE DYNAMICS IN UNSTABLE STRATIFICATION

Our observations of a spherical body suggest that the dissolution of the underside is strongly affected by the flows associated with the unstable density profile near the surface. In particular, the solute-laden fluid near the surface sits above less-dense ambient fluid and this gravitationally unstable stratification is continually fed by the dissolution process, leading to fine-scale plumes that combine to form a turbulent descending jet. Here we carry out additional experiments aimed at understanding the role of the initial geometry in determining the local material loss rate and dynamics of the receding boundary for this case of dissolution in an unstable stratification. We consider a family of wedge shapes that allow the exploration of differently sloped flat surfaces in a quasi-two-dimensional (quasi-2D) setting. We also study additional bodies chosen in order to compare the dissolution dynamics of quasi-2D shapes with their 3D axisymmetric analogs.

#### A. Wedge geometries: The role of shape in quasi-2D dissolution

To examine the effect of shape on dissolution of the lower surface of an object, we study wedges of triangular cross section that are immersed point-downward within water. This family of shapes allows for the systematic variation of the surface inclination relative to gravity by considering wedges of differing base angles. For these experiments, the opening angle  $\theta$  at the base of the wedge is varied between  $60^\circ$  and  $110^\circ$  in  $10^\circ$  increments and these bodies are realized using custom-built molds. The length of each body is several times greater than the height and width of its triangular profile, ensuring a quasi-two-dimensional setting. The body is supported by an embedded rod that runs the entire length. Using the lighting and camera as described for the spherical body, we capture the cross-sectional profile over time, and examples of the shape evolution for  $60^\circ$  and  $100^\circ$  wedges are shown in Fig. 5. To extract each shape profile, we examine the intensity in each image, which is found to fluctuate near the lower boundary of the body because variations in sugar concentration cause variations in refractive index. For this reason, we first apply a circular filter of size comparable to the spatial intensity fluctuations (less than 1 mm) and this smoothed or blurred image is then thresholded to identify the outline of the body. This technique is expected to faithfully report on the overall shape but not the fine-scale features. A time-lapse video of a dissolving wedge is included as video S3 in Ref. [38].

These experiments reveal two key features of the shape evolution: (i) the underside of each body becomes rough and pitted and (ii) the overall shape of each remains nearly constant as it shrinks. The pitting is best illustrated in a photograph of the undersurface of a partially dissolved wedge that has been removed from the water, as shown in Fig. 6. These features are millimeters in scale and are reminiscent of the patterns seen in previous experiments on horizontal surfaces undergoing dissolution [31]. To quantitatively assess the second observation, we measure the variation over time in the base angle of the wedge for many different initial angles. This is achieved by fitting two lines to each side of the lower half of the wedge and measuring the angle between them. These data are



FIG. 6. Small-scale roughness on the underside of a partially dissolved wedge. The wedge has dissolved for 10 min and the scale bar is 1 cm.

displayed in Fig. 7(a), with two trials carried out for each initial base angle. The time traces are remarkably constant in time, showing that in all cases the initial shape is retained throughout the dissolution process. These dynamics thus display a near perfect memory.

To further characterize the retention of the initial geometry, we consider normalized forms for the base angle and for the temporal progression of the dissolution process. The base angle measured at any instant can be normalized by its initial value  $\theta/\theta_0$ , a ratio that readily quantifies deviations. We plot this against the quantity  $1 - A/A_0$ , where  $A$  is the cross-sectional area of the body at any instant and  $A_0$  is the initial cross-sectional area. This quantity indicates the amount of material removed, taking on a value of 0 at the beginning and proceeding to 1 when the body vanishes. In Fig. 7(b) we display the dynamics for all bodies using these variables. The variation in the base angle is remarkably small, with systematic deviations typically on the order of a few percent even as the bodies shrink to 10% of their original size. The larger and seemingly random deviations seen at late times are due to errors in measuring the angle because of the shorter side lengths. The runtime of the experiments are typically limited by exposure of the embedded support rod as the body dissolves.

The constant shape angle seen in the data of Fig. 7 indicates that the speed of recession of the lower surfaces, and thus the local dissolution rate, is uniform and does not vary for different positions. To assess this, we use the time sequence of the extracted shape outlines to determine the local normal velocity of the interface at each location and at each instant in time. Our method considers a given time  $t$  and a location along the associated interface that is given by a normalized arc length  $s$ , which is defined to start at 0 at the upper left corner of each profile, increases as one winds clockwise around the profile, and attains the value of 1 upon returning to the corner. The local normal distance  $\Delta y$  between the given interface at time  $t$  and the previous interface at time  $t - \Delta t$  is determined by the projection of a perpendicular line between these interfaces. An estimate of the local normal velocity is then given by  $V_n(s, t) = \Delta y / \Delta t$  at arc length location  $s$  and time  $t$ .

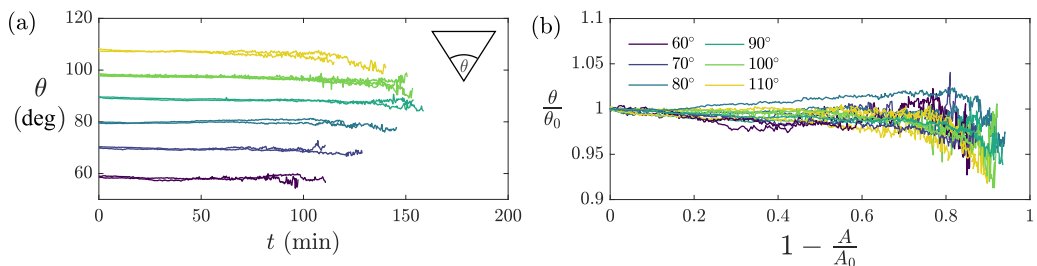


FIG. 7. Shape memory in dissolving wedges. (a) Evolution of the base angle for wedges of differing initial angles. (b) Angle of the wedge normalized by the initial angle as a function of the change in area, normalized by the initial area.

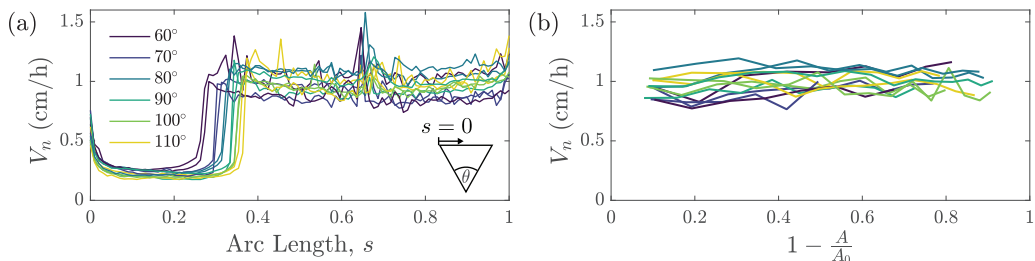


FIG. 8. Dissolution velocity on the lower side is constant with space and time. (a) Dissolution velocity as a function of arc length around a triangular wedge, averaged over time. (b) Average dissolution velocity on the lower side of a triangular wedge as a function of the change in area, normalized by the initial area.

The results of this analysis are shown in Figs. 8 and 9, where we show the space and time averages of  $V_n(s, t)$  for wedges of different base angles. When averaged over time for each location  $s$  on each wedge of base angle  $\theta$ , one arrives at the curves shown in Fig. 8(a). The regions of low dissolution rate correspond to the upper surfaces of each body and a higher rate occurs on the two lower sides. For any given body, it can be seen that the dissolution rate on the underside is approximately uniform in space and does not vary systematically with  $s$ . We also note that the dissolution rate is significantly larger, by about four times, on the lower surfaces than the upper, which we attribute to the flows associated with unstable stratification. To examine possible changes in time of the dissolution rate, we plot in Fig. 8(b) the spatially averaged normal velocity versus  $1 - A/A_0$ . No clear trends in these data are evident, indicating that the dissolution rate of the lower boundaries is relatively constant in time. Finally, we assess the dependence of the dissolution rate, as quantified by the time- and space-averaged normal velocity, on the initial base angle of the wedge, as shown in Fig. 9. These results show no discernible trend, indicating that the dissolution rate is insensitive to the inclination angle over the range investigated.

Taken together, these experiments show that, for a wedge dissolving from below, the dissolution rate does not significantly vary over time, or with position along the surface, or with the initial base angle of the wedge for the range of angles investigated. For the flat surfaces considered here, the apparent independence of rate on location along the surface is sufficient to ensure that the initial shape is preserved throughout the evolution. For this case of dissolution from below, the dynamics can thus retain a near perfect memory of the initial conditions.

### B. Comparing quasi-2D and 3D axisymmetric geometries

To test whether the retention of the initial shape is a general characteristic of dissolution from below, we next consider additional quasi-2D geometries as well as their 3D axisymmetric

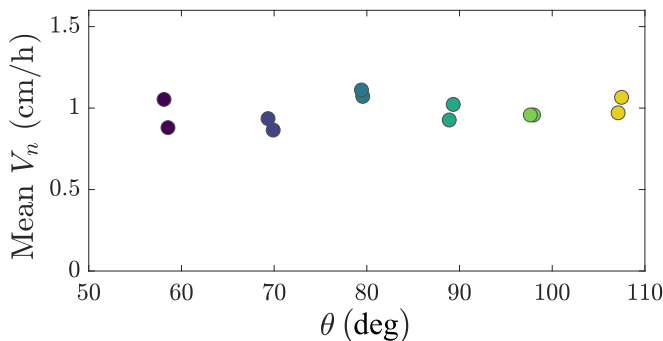


FIG. 9. Mean dissolution rate on the lower side varies little with base angle  $\theta$ .

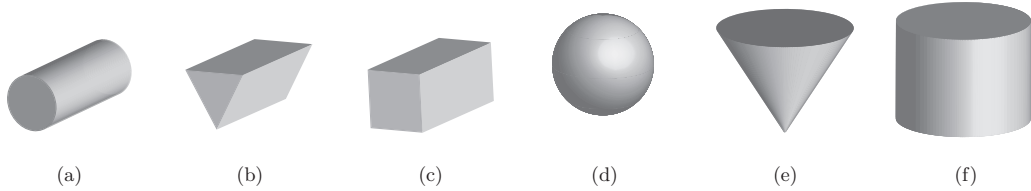


FIG. 10. Quasi-2D and 3D axisymmetric geometries. Horizontal cylinder of (a) circular, (b) triangular, and (c) rectangular cross sections. Analogous 3D solids of revolution include (d) a sphere, (e) a cone, and (f) an upright cylinder.

analogs. In particular, we consider quasi-2D settings given by extended bodies or generalized cylinders whose cross sections are circular and rectangular, in addition to the triangular (wedge) case discussed above. These bodies and their orientation for these experiments are illustrated in Figs. 10(a)–10(c). The corresponding 3D axisymmetric analogs are surfaces of revolution formed by rotating these cross sections about a vertical axis, yielding the sphere introduced earlier but also a cone (pointed downward) and a squat vertical cylinder. These shapes and their orientations are illustrated in Figs. 10(d)–10(f). For both 2D and 3D settings, these three geometries are chosen in order to compare lower surfaces that are rounded, flat but inclined relative to gravity, and flat and horizontal, respectively. All bodies are again generated in custom molds, immersed in water, and then photographed while backlit in order to extract the time evolution of shape.

For all these initial geometries, the measured cross-sectional shapes over time are plotted at 10-min intervals in Fig. 11. Revisiting the case of a quasi-2D wedge in Fig. 11(b), here of base angle  $\theta = 60^\circ$ , we see that the lower surface is marked by uniform recession rate and thus the retention of the initial shape. The 3D analog is a cone and the shape dynamics of Fig. 11(e) show that the uniform rate and retention of initial shape are again features of the dissolution process. This suggests that the three

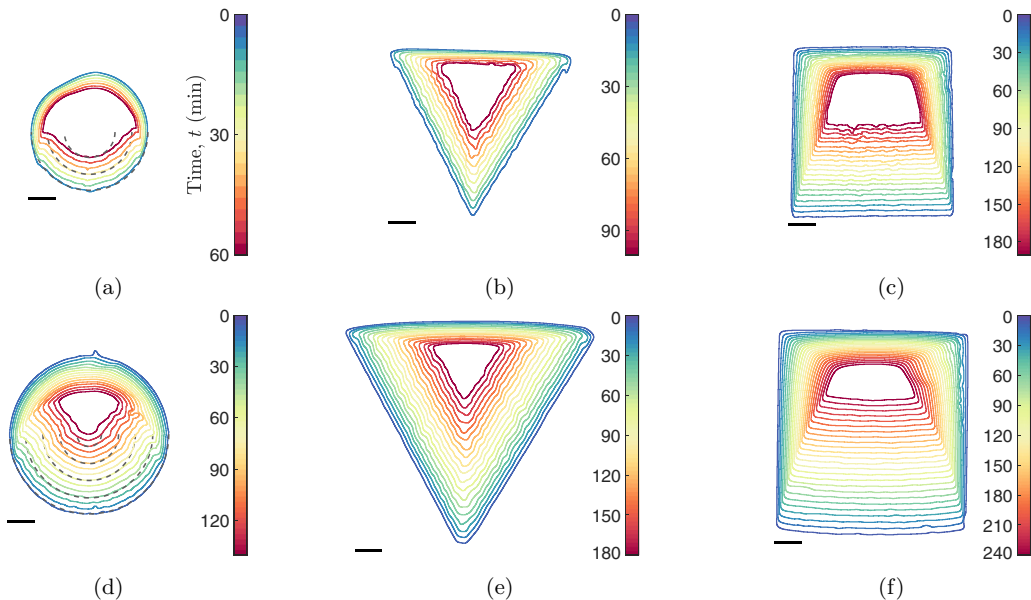


FIG. 11. Comparing shape evolution of quasi-2D and 3D bodies. The initial shapes correspond to those of Fig. 10, with (a)–(c) 2D cylindrical geometries and (d)–(f) 3D solids of revolution. The wedge and cone have  $60^\circ$  base angle. In all cases, cross-sectional profiles are shown every 10 min and the scale is 1 cm.

dimensionality and nonzero curvature (due to curvature in the horizontal plane) do not undermine the shape memory.

The cases of a rectangular extended body, whose dynamics are given in Fig. 11(c), and its 3D analog of an upright circular cylinder shown in Fig. 11(f) are both examples in which the initial lower surface is flat and horizontal. Again, we see that the later forms of the lower surface do not differ substantially from the initial form. That these shapes share this property with the family of wedges considered earlier may be understood by noting that a flat horizontal bottom is somewhat analogous to a wedge whose base angle approaches  $180^\circ$ .

The cases of an extended body of circular cross section (i.e., horizontal cylinder) and its 3D counterpart of a sphere, whose dynamics are shown in Figs. 11(a) and 11(d), respectively, are examples of rounded lower surfaces. Here we find that the measured dynamics are consistent with a nearly uniform dissolution rate along the lower surfaces, which corresponds to retention of overall shape. To better see this, in Figs. 11(a) and 11(d) we have overlaid on the measured profiles several dashed arcs indicating how the lower surface would move upward if it were to evolve from its initial arclike shape with exactly uniform normal velocity. The measured dynamics are consistent with this evolution over much of the lower surface, with the exception of the regions just below the cliff or ledge. The deviation from uniform recession in these regions may in part be an artifact of the optical distortion discussed in Sec. II and may reflect actual changes in the local dissolution rate. The rate may be affected by the separation of the flow on the upper surface, an influence that would change in time since the apparent separation point (the cliff itself) is moving. Alternatively, or perhaps additionally, the dissolution rate may substantially differ in these steeply sloped regions from the more gently sloped regions elsewhere on the underside.

These additional experiments show that the retention or memory of the initial geometry for dissolution from below is a robust property that is not sensitive to factors such as surface inclination, dimensionality, or curvature in the horizontal plane. Further, examination of all the data shown in Fig. 11 shows that the evolution of a lower surface is characterized by a typical recession velocity of about 1 cm/h and this dissolution rate is also robust across geometries.

### C. Visualizing flows in quasi-1D dissolution experiments

The quasi-2D and 3D axisymmetric situations discussed above establish that the coupled shape-flow interaction due to dissolution from below can retain memory of the initial state. This property is closely tied to the uniform dissolution rate over the lower surface. That different surface locations recede at similar speeds suggests that they share similar flow conditions, that is, that the flows driving dissolution near the surface are local and of fine scale. This picture is consistent with the shadowgraph imaging discussed in Sec. II, although the near-body flows on the lower surface of the spherical body are not clearly resolved. To better visualize these flows and determine their scale, we next consider a quasi-one-dimensional scenario in which a thin wire coated with hard candy is held horizontally in water. In this case, the dense solute-laden fluid is expected to form a sheetlike jet that descends, and shadowgraph imaging through this sheet can be used to reveal the structure of this flow.

In Figs. 12(a) and 12(b) we show example shadowgraph images captured soon after insertion of this quasi-1D body and later in the dissolution process when a steady state is reached. The images show that not only is the dissolved material confined to a quasi-2D sheet below the body, but this sheet displays fine-scale quasiperiodic structures. Because spatial variations in image intensity in a shadowgraph correspond to the second derivative of the density field [40], the light and dark vertical stripes in Fig. 12 indicate positive and negative horizontal density gradients, which we interpret as narrow vertical plumes of dense fluid. The impression of thin descending plumes is readily observed in a movie of this process, available as video S4 in Ref. [38]. Close inspection of these images and videos reveals that the plumes have a horizontal length scale of approximately 0.5–1 mm. This confirms the picture that the flows driving dissolution on the underside of a surface are local and of a scale far smaller than the size of the bodies studied throughout this work.

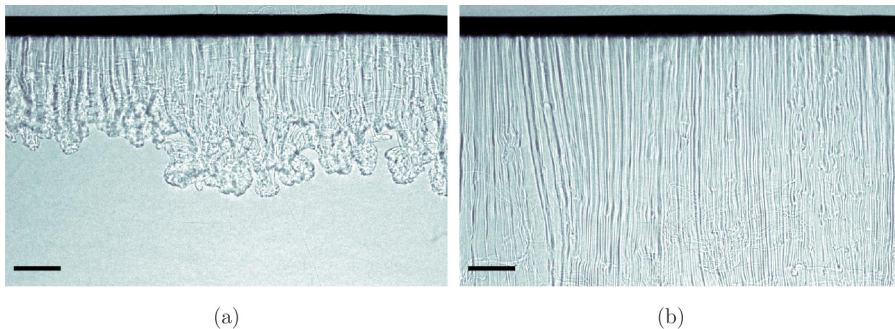


FIG. 12. Millimeter-scale plumes descend from a quasi-1D geometry. Shadowgraph images of wire coated in candy, whose dissolution in water results in fine-scale plumes descending under gravity: (a) startup of flow and (b) long-term behavior. The scale bar is 1 cm.

#### D. Theoretical estimates for the plume size and dissolution velocity

Our observations suggest that local flows in the form of fine-scale plumes drive the local pitting and uniform recession of the underside of a dissolving body. To offer additional support, we use these ideas to furnish theoretical estimates for the plume size, to be compared to the millimeter-scale plumes and pitting patterns seen in experiments, as well as the typical dissolution velocity, which is found to be on the order of 1 cm/h for a wide variety of conditions. Our theoretical estimates stem from the following picture: When dissolution is initiated on the underside of a body, a layer of dense solute-laden fluid grows until reaching a critical thickness at which it undergoes the Rayleigh-Taylor instability, overturning locally to form quasiperiodic drips. We associate the horizontal wavelength of the instability with the size scale of the plumes and surface pitting, and the dissolution velocity can be estimated by considering the rate of diffusion across a fluid layer of the critical thickness.

We first seek an estimate the critical thickness  $\delta_c$  of the concentration boundary layer that triggers the instability, which occurs when viscous forces are no longer sufficient to damp out disturbances [41,42]. For a fluid layer with one rigid and one free boundary [43], this occurs at a critical value of the Rayleigh number given by

$$\text{Ra}_c = \frac{g \Delta \rho \delta_c^3}{\nu \rho_f D} = 1101, \quad (1)$$

where  $g = 9.8 \text{ m/s}^2$  is gravitational acceleration,  $\Delta \rho$  the density difference across the layer,  $\nu$  the kinematic viscosity,  $\rho_f$  the density of the far-field fluid, and  $D$  the molecular diffusion constant of the dissolved species. The solute concentration profile, which dictates the density difference, is assumed to have  $c_s = 1$  within the solid,  $c_i$  at the solid-fluid interface, and then decrease from  $c_i$  to the far-field fluid value of  $c_f = 0$  over the thickness  $\delta_c$ . We take  $c_i$  to be the saturation concentration.

The above formula applies to a solution in which the density alone is affected by the nonhomogeneous concentration, while our experiments involve properties, such as viscosity, that vary with sugar concentration. Nonetheless, order-of-magnitude estimates can be furnished by approximating the relevant parameter values or range of values. (i) The densities of pure solid and fluid are directly measured to be  $\rho_s = 1.4 \text{ g/cm}^3$  and  $\rho_f = 1.0 \text{ g/cm}^3$ . (ii) Assuming the saturation concentration value for pure sucrose at room temperature [44], we take  $c_i = 0.67$ . This, along with a linear density-concentration relationship of  $\rho = \rho_f + (\rho_s - \rho_f)c$ , yields  $\Delta \rho = \rho(c_i) - \rho(c_f) = 0.3 \text{ g/cm}^3$ . (iii) The viscosity in the boundary layer is expected to vary between that of saturated sucrose solution,  $\nu_i = 7.7 \times 10^{-4} \text{ m}^2/\text{s}$ , and that of water,  $\nu_f = 1.0 \times 10^{-6} \text{ m}^2/\text{s}$ . As shown below, this 770-fold difference corresponds to a far smaller variation in the estimate of  $\delta_c$ . (iv) We assume a value of the coefficient of diffusion relevant to dilute sucrose in water,  $D = 4.3 \times 10^{-10} \text{ m}^2/\text{s}$  [45]. We have made use of some parameter values for pure sucrose, a main component of candy along with long-chain sugars.

Putting in these approximate values yields

$$\delta_c = \left( \frac{\text{Ra}_c \nu \rho_f D}{g \Delta \rho} \right)^{1/3} = 0.06\text{--}0.6 \text{ mm}, \quad (2)$$

where the range of values reflects the extremes in viscosity from that of pure water to saturated sucrose solution. Roughly speaking, it is this small thickness that sets the horizontal wavelength of the instability. A more refined computation [46] shows that, for high Schmidt numbers, here estimated as  $\text{Sc} = \nu/D \approx 10^3$  using parameters for dilute sucrose solution [45], this wavelength is several times longer than the critical thickness, namely,  $\lambda_c \approx 5\delta_c = 0.3\text{--}3 \text{ mm}$ . This result corresponds to the most-unstable wavelength that develops for diffusion into an initially solute-free fluid below [46]. The range of  $\lambda_c$  values corresponds well with the experimentally observed length scales for the plume spacing and the surface pits, corroborating the picture that local flows drive dissolution of an undersurface.

The quantity  $\delta_c^2/D$  represents the time it takes the solute in the boundary layer to diffuse to the critical thickness for instability. One might associate this with the growth of the boundary layer to the point that a solute-laden plume is released from the surface. For the conditions studied here,  $\delta_c \sim 0.1 \text{ mm}$  and  $D = 4.3 \times 10^{-10} \text{ m}^2/\text{s}$  yields  $\delta_c^2/D \sim 10 \text{ s}$ . This is fast compared to the timescales investigated in our experiments, offering an explanation for the near constancy of the dissolution velocity seen in Fig. 8(b).

Additional support for this picture of the near-body flow comes from estimating the typical normal velocity  $V_n$  of the underside of a dissolving body, which is found to be  $1 \text{ cm/h}$  in experiments. Conservation of solute material across the solid-fluid interface demands that

$$\rho_s(c_i - c_s)V_n = -\rho_f D \frac{\partial c}{\partial n}, \quad (3)$$

where  $\partial c/\partial n$  represents the concentration gradient normal to the surface [47]. The left-hand side is the material flux from the receding solid to the fluid at the interface and the right-hand side employs Fick's law of diffusion to account for the flux from the interface to the fluid below. Approximating the gradient evaluated at the interface by an average over the boundary-layer thickness  $\partial c/\partial n \approx (c_i - c_f)/\delta_c$ , we arrive at

$$V_n = \frac{\rho_f D}{\rho_s \delta_c} \frac{(c_i - c_f)}{(c_s - c_i)} \approx 0.4\text{--}4 \text{ cm/h}, \quad (4)$$

which again successfully accounts for the experimental observations.

#### IV. DISSOLUTION FROM ABOVE: SHAPE DYNAMICS IN STABLE STRATIFICATION

We next take up the case of dissolution of a body's upper surface, that is, the recession of a boundary that is dissolving into the fluid above. The initial body shapes studied so far allow the upper surface to evolve relatively little, as the underside recedes several times faster and thus dominates the material loss. To remedy this, we next consider tall upright bodies that are supported on a lower platform, thus presenting ample material to be dissolved from above while eliminating any dissolution from below. We focus again on analyzing the recession dynamics of the surface and especially how the terminal state depends on the initial geometry. We expect that the stable stratification near the surface, and thus attached boundary-layer flows, will lead to quite different results from those observed for the underside of a body.

##### A. Dissolution of a slender axisymmetric body

We first cast molten candy within tall cylinders of approximate height  $25 \text{ cm}$  and diameter  $3.5 \text{ cm}$ . We find that if such a body is placed upright in water, it inevitably develops one or more cavities on the side that rapidly grow, carving through the body and leading to the collapse of the material

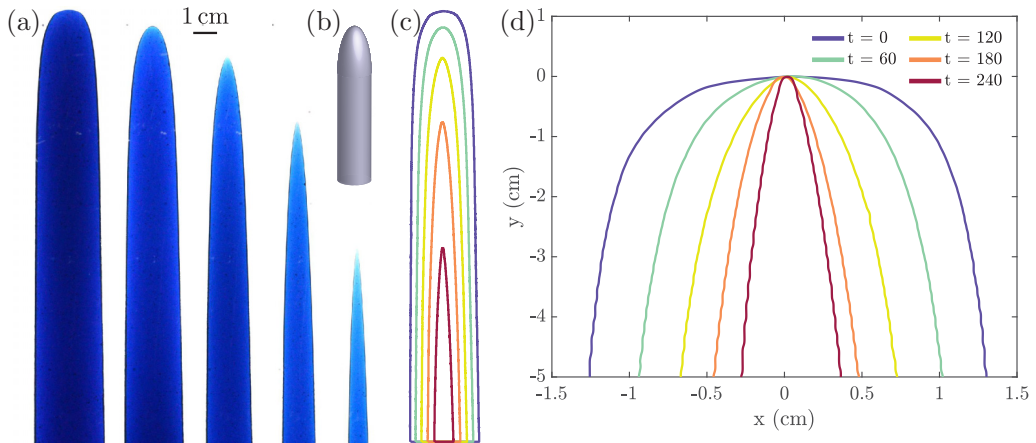


FIG. 13. Shape evolution of a tall axisymmetric body dissolving within water. (a) Photographs shown at 60-min intervals. (b) Sketch of the initial geometry. (c) Extracted cross sections shown every 60 min and at the same scale as images in (a). (d) Zoomed-in and rescaled profiles of the tip region, with all contours shifted to place the tip at the origin.

above. These cavities seem to start at surface defects, perhaps caused by slightly nonvertical walls of the mold or by the presence of a bubble during casting, and expand relatively rapidly because they present an under surface that, as our previous results show, is subject to high dissolution rates. To overcome this problem, we reshape the surface of the candy cylinder using a lathe, which spins the body about its long axis as we manually apply a wet sponge. In this way, we are able to remove surface defects and give the body a rounded top and gentle taper along its length, ensuring that it dissolves from above at all surface locations. The resulting axisymmetric shape is shown in the schematic of Fig. 13(b) and the initial shape of the actual body is captured in the first photograph of Fig. 13(a).

The dissolution dynamics within water of such a body is shown by the photographs of Fig. 13(a) that represent snapshots taken every 60 min and video S5 in Ref. [38] is added to visualize the dissolution process. The corresponding cross-sectional profiles extracted from these images are overlaid in Fig. 13(c). In contrast to the case of dissolution of lower surfaces, here we find that the surface does not display any pitting but rather remains smooth. These data also show that the overall shapes form an upward-pointing spike whose tip seems to sharpen over time. To examine this evolution in more detail, we plot in Fig. 13(d) these same profiles zoomed-in and overlaid with respect to the tip location, which corresponds to a reference frame comoving with the descending tip. The widened aspect ratio of the plot axes also serves to accentuate changes in shape. This succession of profiles clearly shows that the tip region becomes ever more slender throughout the dissolution process, with no clear plateau evident. Thus, the evolution seems to lose memory of the initial blunt tip and attain an ever-sharpening terminal state.

### B. The effect of initial conditions

To examine the effect of initial conditions, we use our reshaping technique to manufacture a body whose tip is initially sharp rather than blunt. As before, this body is smoothed and tapered to ensure dissolution from above at all locations, and the initial shape is represented in the schematic of Fig. 14(b). In Fig. 14(a) we show the extracted cross-sectional profiles obtained from experiments, where snapshots are shown every 60 min. Here again we see a spikelike geometry whose tip descends during dissolution, and in Fig. 14(b) we examine the shape dynamics zoomed-in and in the frame of the tip. The early profiles show that the initially sharp tip is widened within the first 60 min (blue to green on colormap), but thereafter we observe a similar tendency to become increasingly slender

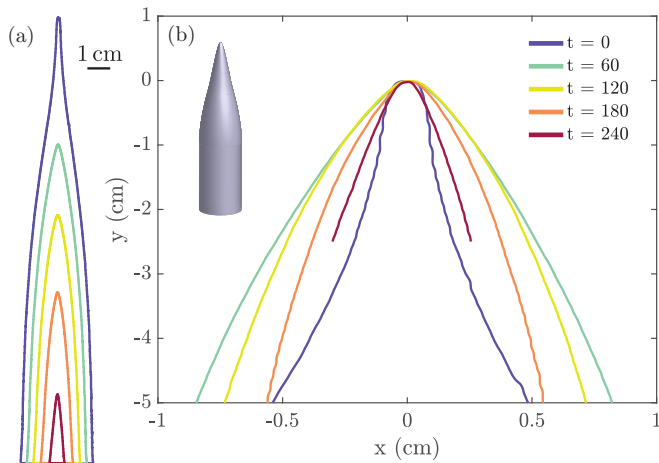


FIG. 14. Sharpened initial shape. (a) Shape profiles shown at 60-min intervals. (b) Zoomed-in, rescaled, and shifted profile shapes to focus on the evolution of the tip. The inset shows a sketch of the initial geometry.

for later times (green to red). This indicates that memory of the initial conditions is again lost as the starting shape is erased en route to the sharpening regime.

### C. Analysis of the tip curvature

To further support the existence of the ever-sharpening terminal state, we use the measured time series of profile shapes for both initial conditions to extract the curvature of the tip over time. Increasing sharpness corresponds to increasing curvature, thus providing a quantitative characterization of the tip shape dynamics.

As curvature is a high-order derivative of shape, we employ a method that first fits a fourth-order polynomial to obtain a smooth curve  $y(x)$  describing the shape of the tip region for each extracted profile. The slope of this fit is used to measure the local angle  $\theta$  of the surface relative to the direction of gravity, as  $\tan(\theta) = \partial x / \partial y$ . This angle as a function of arc length  $s$  along the surface is plotted for the initially blunt body in Fig. 15(a) and for the sharpened body in Fig. 15(b). It can be seen that late in the evolution the angle is close to vertical each side of the tip, abruptly switching between  $\pi$  and 0 in the region close to the tip. The steep derivative of  $\theta$  with respect to  $s$  corresponds to a high principle curvature  $\kappa = d\theta/ds$ . A similarly steep drop in  $\theta$  is seen for the sharper initial condition data of Fig. 15(b).

The evolution in time of the tip curvature  $\kappa(s = 0)$  is shown in Fig. 15 for the initial conditions of a blunt tip (blue curve) and a sharp tip (red). The case of a blunt initial profile shows an ever-increasing curvature over time and in fact the curvature seems to be increasing at an increasing rate (i.e., the second derivative is positive). The case of a sharpened initial tip shows that the curvature initially decreases before later arriving at a state of ever-increasing curvature. The curvature plots for these different initial conditions also seem to coincide for these later times and attain similarly high values towards the end, indicating an example of convergent dynamics that are not sensitive to initial conditions.

At later times, the accuracy of our shape extraction is limited by the poor contrast of the exceedingly thin body against the background. This artificially blunts the tip region and thus the curvature values reported for later times in Fig. 15 may be viewed as underestimates. Nonetheless, the maximal values of about  $20 \text{ mm}^{-1}$  are impressively high. To give a sense for the fineness of the tip, we note that such a curvature value corresponds to a radius of curvature of 0.05 mm, which is of the same order as the thickness of a sheet of paper or the width of a human hair.

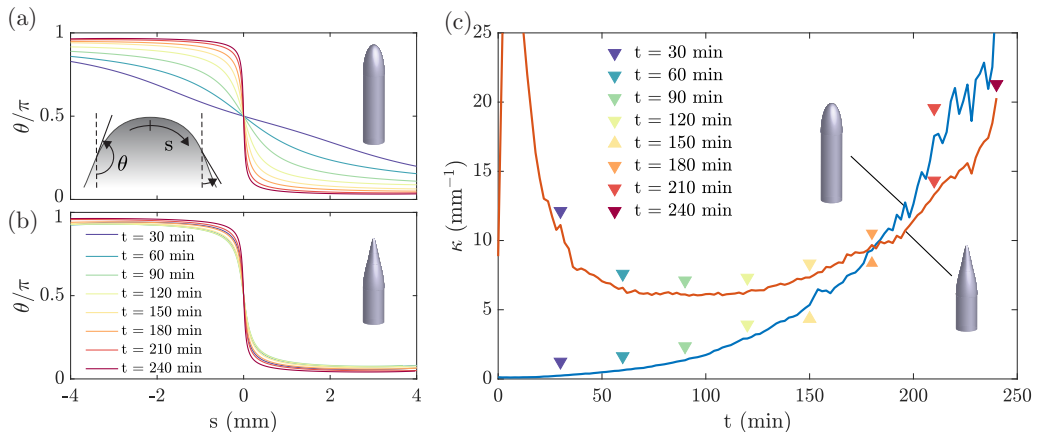


FIG. 15. Tip curvature continuously increases at later times. The angle  $\theta$  of the surface with respect to gravity is plotted vs arc length  $s$  near the tip for (a) an initially blunt body and (b) a sharpened body. (c) Time evolution of the principal curvature  $\kappa(s=0)$  at the tip for initially blunt (blue) and sharpened (orange) bodies.

These experiments show that, regardless of initial conditions, a body dissolving from above tends toward an ever-sharpening state marked by increasing tip curvature. This is an example of memoryless dynamics in which the initial conditions are erased en route to a terminal state and this differs strikingly from the near perfect memory or retention of initial conditions observed for dissolution from below.

## V. DISCUSSION

These experiments on the shape evolution of dissolvable bodies with simple initial geometries show markedly different outcomes depending on the inclination of the surface relative to gravity. Surfaces dissolving from below, such as the underside of a body, can recede uniformly and thus retain their initial shape. We find that this shape memory property holds across flat surfaces for a wide range of inclinations and approximately so for rounded surfaces. In contrast, an upper surface dissolving into the fluid above tends to lose memory of its initial shape and forms a spikelike structure that ever sharpens in time.

These two cases are accompanied by very different flow conditions that help to explain their different shape dynamics. The character of the near-surface flow is largely determined by the gravitational stability of the fluid. For the underside of a body, the arrangement of dense solute-laden fluid above less-dense fresh fluid is gravitationally unstable and the concentration boundary layer undergoes the Rayleigh-Taylor instability, locally overturning and forming narrow plumes that descend. Our experiments and theoretical estimates indicate that the length scale of the instability is on the order of a millimeter, which is small in comparison to the body sizes studied here. Evidence for fine-scale flows can also be found in previous works of dissolution into fluid below [28–31,48]. Our visualization studies show that it is these localized flows that carry solute downward and away from the surface and there seems to be little communication or influence among different surface locations. Thus the surface recedes nearly uniformly and the initial shape is preserved.

For an upper surface dissolving into the fluid above, on the other hand, the concentration boundary layer is gravitationally stable and the flow remains attached. In this case, we expect communication between different surface locations, as material dissolved at any point is conveyed by the flow downward along the body [49]. Thus, the flows driving dissolution are inherently global and extend over the entire surface and the concentration boundary-layer profile is likely to vary at different locations. Hence we expect nonhomogeneous dissolution rates and accompanying changes in shape.

Indeed, the shape dynamics observed in our experiments share qualitative similarities with previous studies on dissolution into fluid above [32]. The reasoning given here offers some explanation for the observed departure from the initial shape and thus a loss of shape memory.

Explaining the ever-sharpening shape observed as the terminal state in our experiments would seem to require a detailed theory and here we posit some preliminary ideas. We first highlight a paradox: The successive interfaces shown in Figs. 13(c) and 14(a) show that dissolution rates tend to be fastest near the tip and yet the tip is not blunted by this action but rather sharpens over time. That dissolution is faster near the top of the body seems consistent with reasoning based on concentration boundary layers [49]. Namely, we expect thin boundary layers near the top where fresh water is fed from above and thicker layers downstream due to the conveyance of dissolved material from all upstream surface locations. As suggested by Fick's law, dissolution rate varies inversely with boundary-layer thickness, thus accounting for the decreasing rate with downstream location. To address the paradox, we must appreciate that the evolution of the shape depends not only on the normal velocity but also on the curvature [50,51], which may vary along the surface. A simple thought experiment is instructive: Consider a profile shape that has vertical sidewalls capped by a semicircular top and evolve this shape inward with uniform local normal velocity. The uniform recession does not preserve shape, as might be naively expected, but rather the top collapses to a point and the walls meet, at which time the tip curvature diverges. Even if the normal velocity were somewhat faster at the top than at lower points, it still seems a corner, and thus infinite tip curvature, would result. More generally, it seems that the interplay of spatially varying curvature and normal velocity is critical to the sharpening, and future work will assess these ideas through a model informed by boundary-layer theory.

Additional future directions pertain to the retention of shape observed here for lower surfaces, a property which also seems to depend on the spatial variations of the normal velocity and curvature. For example, shape is preserved if the normal velocity and curvature are both uniform, e.g., a self-similarly shrinking circle or sphere. Shape is also preserved if the velocity is uniform and changes in curvature are confined to singular points or corners, e.g. a polygonal body. A surface with continuously varying curvature, however, is only preserved with particular spatial variations in normal velocity. For this reason, future experiments might investigate the dissolution from below of bodies with nonuniform curvature, e.g., a sinusoidal boundary, which would not retain its shape if the normal velocity were found to be uniform. Another future direction is the effect of increasing the viscosity or decreasing the density difference between the solid and fluid. This would have the effect of increasing the length scale associated with the instability on the underside of a shape [cf. Eq. (2)]. If the length scale were increased to be comparable to the size of a dissolving shape, we would expect different dynamics that reflect a more global coupling of the shape and flow. Future studies might also investigate nearly vertical lower surfaces, e.g., for wedges of  $\theta \gtrsim 0$ . For sufficiently steep surfaces, it may be that the boundary-layer flow remains attached over an appreciable portion of the body, in which case our theoretical considerations of separated flow triggered by the Rayleigh-Taylor instability would not apply. Should the boundary-layer thickness vary along the surface, then one expects nonuniform recession velocity and consequent changes in shape, in contrast to the retention of shape seen for larger  $\theta$  (Fig. 7).

The dissolution dynamics and coupled flow-structure evolution studied here is also at work in natural and industrial processes and we may posit some implications and applications. In nature, karst topographies arise from dissolution and display a rich variety of forms [3]. For example, so-called stone forests consist of tall pillars [52] that are perhaps analogous to the vertical spikelike sculptures formed in our experiments on dissolution of an upper surface. The caverns typical of karst are likely carved out by dissolution within a water-filled cavity [3], which we expect to grow primarily by dissolving of the ceiling where unstable density profiles can lead to strong flows. Icebergs and ice shelves represent additional natural analogs, and surface pitting and scallops on their undersides may indicate flow instabilities [30]. Finally, the ever-sharpening regime observed here for dissolution of an upper surface might be applied towards manufacturing structures of extreme fineness.

## ACKNOWLEDGMENTS

We acknowledge support to M.S.D.W. from the US–UK Fulbright Commission and Lloyds of London. The authors would like to thank the two anonymous referees for their helpful and valuable comments.

- 
- [1] M. B. Short, J. C. Baygents, and R. E. Goldstein, Stalactite growth as a free-boundary problem, *Phys. Fluids* **17**, 083101 (2005).
  - [2] L. B. Leopold and M. G. Wolman, River meanders, *Bull. Geol. Soc. Am.* **71**, 769 (1960).
  - [3] A. N. Palmer, Origin and development of limestone caves, *Geol. Soc. Am. Bull.* **103**, 1 (1991).
  - [4] A. Wesley Ward, Yardangs on Mars: Evidence of recent wind erosion, *J. Geophys. Res.* **84**, 8147 (1979).
  - [5] A. E. Scheidegger, A physical theory of the formation of hoodoos, *Geophys. Pura Appl.* **41**, 101 (1958).
  - [6] F. Charru, B. Andreotti, and P. Claudin, Sand ripples and dunes, *Annu. Rev. Fluid Mech.* **45**, 469 (2013).
  - [7] S. Feldman, On the instability theory of the melted surface of an ablating body when entering the atmosphere, *J. Fluid Mech.* **6**, 131 (1959).
  - [8] F. Verniani, On meteor ablation in the atmosphere, *Nuovo Cimento* **19**, 415 (1961).
  - [9] E. Heitz, Chemo-mechanical effects of flow on corrosion, *Corrosion* **47**, 135 (1991).
  - [10] Y. L. Hao and Y.-X. Tao, Melting of a solid sphere under forced and mixed convection: Flow characteristics, *J. Heat Transfer* **123**, 937 (2001).
  - [11] Y. L. Hao and Y.-X. Tao, Heat transfer characteristics of melting ice spheres under forced and mixed convection, *J. Heat Transfer* **124**, 891 (2002).
  - [12] J. A. Neufeld, R. E. Goldstein, and M. G. Worster, On the mechanisms of icicle evolution, *J. Fluid Mech.* **647**, 287 (2010).
  - [13] L. Ristroph, M. Nicholas J. Moore, S. Childress, M. J. Shelley, and J. Zhang, Sculpting of an erodible body by flowing water, *Proc. Natl. Acad. Sci. USA* **109**, 19606 (2012).
  - [14] M. Nicholas J. Moore, L. Ristroph, S. Childress, J. Zhang, and M. J. Shelley, Self-similar evolution of a body eroding in a fluid flow, *Phys. Fluids* **25**, 116602 (2013).
  - [15] F. H. Garner and R. W. Grafton, Mass transfer in fluid flow from a solid sphere, *Proc. R. Soc. London Ser. A* **224**, 64 (1954).
  - [16] T. J. Hanratty, Stability of surfaces that are dissolving or being formed by convective diffusion, *Annu. Rev. Fluid Mech.* **13**, 231 (1981).
  - [17] G. Daccord, Chemical Dissolution of a Porous Medium by a Reactive Fluid, *Phys. Rev. Lett.* **58**, 479 (1987).
  - [18] R. C. Kerr, Convective crystal dissolution, *Contrib. Mineral. Petrol.* **121**, 237 (1995).
  - [19] M. C. Malin and K. S. Edgett, Evidence for recent groundwater seepage and surface runoff on Mars, *Science* **288**, 2330 (2000).
  - [20] V. R. Baker, Water and the martian landscape, *Nature (London)* **412**, 228 (2001).
  - [21] G. Domokos and D. J. Jerolmack, How river Rocks round: Resolving the shape-size paradox, *PLoS One* **9**, e88657 (2014).
  - [22] R. Huggett, *Fundamentals of Geomorphology* (Routledge, New York, 2007).
  - [23] M. B. Short, J. C. Baygents, and R. E. Goldstein, A free-boundary theory for the shape of the ideal dripping icicle, *Phys. Fluids* **18**, 083101 (2006).
  - [24] B. F. Edwards and D. H. Smith, River meandering dynamics, *Phys. Rev. E* **65**, 046303 (2002).
  - [25] J. M. Huang, M. Nicholas J. Moore, and L. Ristroph, Shape dynamics and scaling laws for a body dissolving in fluid flow, *J. Fluid Mech.* **765**, R3 (2015).
  - [26] V. G. Levich, *Physicochemical Hydrodynamics* (Prentice Hall, Englewood Cliffs, 1962), Vol. 69.
  - [27] P. N. Blumberg and R. L. Curl, Experimental and theoretical studies of dissolution roughness, *J. Fluid Mech.* **65**, 735 (1974).
  - [28] R. C. Kerr, Dissolving driven by vigorous compositional convection, *J. Fluid Mech.* **280**, 287 (1994).
  - [29] Y. Liu, L. Ning, and R. Ecke, Dynamics of surface patterning in salt-crystal dissolution, *Phys. Rev. E* **53**, R5572 (1996).

- [30] C. Cohen, M. Berhanu, J. Derr, and S. Courrech du Pont, Erosion patterns on dissolving and melting bodies, *Phys. Rev. Fluids* **1**, 050508 (2016).
- [31] T. Sullivan, Y. Liu, and R. Ecke, Turbulent solutal convection and surface patterning in solid dissolution, *Phys. Rev. E* **54**, 486 (1996).
- [32] E. Nakouzi, R. E. Goldstein, and O. Steinbock, Do dissolving objects converge to a universal shape? *Langmuir* **31**, 4145 (2015).
- [33] A. W. Woods, Melting and dissolving, *J. Fluid Mech.* **239**, 429 (1992).
- [34] T. L. Bergman and F. P. Incropera, *Fundamentals of Heat and Mass Transfer* (Wiley, New York, 2011).
- [35] C. R. Vanier and C. Tien, Free convection melting of ice spheres, *AIChE J.* **16**, 76 (1970).
- [36] H. E. Huppert and J. Stewart Turner, Ice blocks melting into a salinity gradient, *J. Fluid Mech.* **100**, 367 (1980).
- [37] W. P. Edwards, *The Science of Sugar Confectionery* (Royal Society of Chemistry, London, 2000).
- [38] See Supplemental Material at <http://link.aps.org/supplemental/10.1103/PhysRevFluids.3.043801> for the time-lapse movie of a spherical candy dissolving in water (video S1), the movie of stratified layers developed during the dissolution process (video S2), the movie of a wedge dissolving in water (video S3), the movie of concentration plumes falling from a dissolving surface (video S4), and the time-lapse movie of an upright cylindrical body dissolving in water with a configuration that is gravitationally stable (video S5).
- [39] G. S. Settles, *Schlieren and Shadowgraph Techniques: Visualizing Phenomena in Transparent Media* (Springer Science + Business Media, New York, 2012).
- [40] D. E. Mowbray, The use of schlieren and shadowgraph techniques in the study of flow patterns in density stratified liquids, *J. Fluid Mech.* **27**, 595 (1967).
- [41] W. Lick, The instability of a fluid layer with time-dependent heating, *J. Fluid Mech.* **21**, 565 (1965).
- [42] L. N. Howard, *Convection at High Rayleigh Number* (Springer, Berlin, 1966), pp. 1109–1115.
- [43] S. Chandrasekhar, *Hydrodynamic and Hydromagnetic Stability* (Dover, New York, 1981), p. 42.
- [44] R. W. Hartel, R. Ergun, and S. Vogel, Phase/state transitions of confectionery sweeteners: Thermodynamic and kinetic aspects, *Compr. Rev. Food Sci. F.* **10**, 17 (2011).
- [45] F. Mohos, *Confectionery and Chocolate Engineering: Principles and Applications* (Wiley, New York, 2010).
- [46] T. D. Foster, Haline convection induced by the freezing of sea water, *J. Geophys. Res.* **73**, 1933 (1968).
- [47] A. J. Wells and M. Grae Worster, Melting and dissolving of a vertical solid surface with laminar compositional convection, *J. Fluid Mech.* **687**, 118 (2011).
- [48] T. Sullivan, W. Brown, M. Kerkel, and R. Ecke, Turbulent convection and surface patterning in solid dissolution, *Phys. Lett. A* **206**, 49 (1995).
- [49] C. Mayes, H. Schlichting, E. Krause, H. J. Oertel, and K. Gersten, *Boundary-Layer Theory* (Springer, Berlin, 2003).
- [50] R. C. Brower, D. A. Kessler, J. Koplik, and H. Levine, Geometrical Approach to Moving-Interface Dynamics, *Phys. Rev. Lett.* **51**, 1111 (1983).
- [51] E. Ben-Jacob, N. Goldenfeld, J. S. Langer, and G. Schön, Dynamics of Interfacial Pattern Formation, *Phys. Rev. Lett.* **51**, 1930 (1983).
- [52] Z. Zhi Gan, Karst types in China, *GeoJournal* **4**, 541 (1980).

*Correction:* An author's name was misrepresented in Refs. [13,14,25] and has been corrected.